

Polarization Transfer to External Nuclear Spins Using Ensembles of Nitrogen-Vacancy Centers


A.J. Healey,^{1,2} L.T. Hall,¹ G.A.L. White¹, T. Teraji,³ M.-A. Sani,⁴ F. Separovic⁴,
J.-P. Tetienne^{1,2,*} and L.C.L. Hollenberg^{1,2,†}

¹*School of Physics, University of Melbourne, VIC 3010, Australia*

²*Center for Quantum Computation and Communication Technology, School of Physics, University of Melbourne, VIC 3010, Australia*

³*National Institute for Materials Science, Tsukuba, Ibaraki 305-0044, Japan*

⁴*School of Chemistry, Bio21 Institute, University of Melbourne, VIC 3010, Australia*

 (Received 28 January 2021; revised 20 April 2021; accepted 22 April 2021; published 24 May 2021)

The nitrogen-vacancy (N-V) center in diamond has emerged as a candidate to noninvasively hyperpolarize nuclear spins in molecular systems to improve the sensitivity of nuclear magnetic resonance (NMR) experiments. Several promising proof-of-principle experiments have demonstrated small-scale polarization transfer from single N-V centers to hydrogen spins outside the diamond. However, the scaling up of these results to the use of a dense N-V ensemble, which is a necessary prerequisite for achieving realistic NMR sensitivity enhancement, has not yet been demonstrated. In this work, we present evidence for a polarizing interaction between a shallow N-V ensemble and external nuclear targets over a micrometer scale, and characterize the challenges in achieving useful polarization enhancement. In the most favorable example of the interaction with hydrogen in a solid-state target, a maximum polarization transfer rate of approximately 7500 spins per second per N-V is measured, averaged over an area containing order 10^6 N-V centers. Reduced levels of polarization efficiency are found for liquid-state targets, where molecular diffusion limits the transfer. Through analysis via a theoretical model, we find that our results suggest that implementation of this technique for NMR sensitivity enhancement is feasible following realistic diamond material improvements.

DOI: [10.1103/PhysRevApplied.15.054052](https://doi.org/10.1103/PhysRevApplied.15.054052)

I. INTRODUCTION

Nuclear magnetic resonance (NMR) underpins a variety of techniques that find use across the fields of physics, chemistry, and the life sciences. The sensitivity of a NMR measurement is proportional to the degree of nuclear spin polarization in the target to be analyzed, which is very low under typical thermal conditions ($P_{\text{th}} \approx 10^{-5}$ at room temperature and a magnetic field of 3 T). Consequently, a number of approaches have been developed to achieve levels of polarization well in excess of thermal levels (“hyperpolarization”) in nuclear spin ensembles. To date, dynamic nuclear polarization (DNP) [1–4] is the most widely implemented method of achieving hyperpolarization, with parahydrogen-induced polarization (PHIP) [5,6] and optical pumping-based [7,8] methods also finding success. These methods, however, are far from being problem-free in their application. Each suffers from limitations, such as in their target specificity (PHIP, optical pumping), or in

the technically challenging conditions required for optimal operation (e.g., cryogenic temperatures, large magnetic fields, and strong microwave driving for DNP).

For these reasons, it has been proposed that the negatively charged nitrogen-vacancy (N-V) center defect in diamond [9] may be a suitable candidate to address some of the shortcomings in other techniques [10–12]. The N-V center’s electron spin is efficiently polarized (approximately 80%) on a microsecond timescale and is easily manipulated at room temperature. Promising proof-of-principle experiments have demonstrated polarization transfer from N-V centers to nuclear targets via the magnetic dipole-dipole interaction using a variety of experimental protocols [10–19]. This transfer is noninvasive to the target and general, avoiding the target specificity limitations of other techniques. Furthermore, the potential for room-temperature and low-field operation raises the prospect of achieving hyperpolarization with a reduced technical overhead. However, work so far has been limited to either internal ^{13}C [13–19] or small-scale external polarization with single N-V centers [10–12], which are naturally limited in their scope towards achieving bulk

*jtetienne@unimelb.edu.au

†lloydch@unimelb.edu.au

hyperpolarization over a sample volume useful for NMR. Recent theoretical work in Ref. [20] showed that bulk NMR enhancement (as well as for N- V -based, micron-scale NMR [21,22]) is possible using dense N- V ensembles with sufficiently good quantum coherence properties. However, successful experimental demonstration of polarization transfer from a N- V ensemble to an external nuclear target has not yet been achieved.

Although N- V ensembles essentially act as many independent N- V centers for the purpose of hyperpolarization [20], extending the previously reported single N- V results to the case of a dense ensemble is not trivial. As the distance between N- V centers and nuclei external to the diamond will be several nanometers, the dipole-dipole coupling that governs the polarization transfer is weak, and thus the N- V coherence time T_2 (which is scheme dependent) emerges as the limiting variable [23]. In increasing the density of N- V centers within the diamond sample, the magnetic noise is increased proportionally, degrading these quantum properties. The dominant noise source in a dense ensemble is the substitutional nitrogen bath [24] that, with current standard sample production techniques, is at minimum 10 times more abundant than the N- V density [25]. In addition, the necessity of placing the N- V centers near the diamond surface brings another significant contribution to N- V decoherence: a range of fast-fluctuating surface defects that render near-surface N- V properties much worse than those in the bulk and result in band bending that reduces the charge stability of the negative N- V charge state within a few nanometers of the surface [26–30].

Furthermore, while it may be possible to find a single N- V located within an anomalously calm spin environment that exhibits unusually long coherence times, or that is situated anomalously close to the surface and thus couples more strongly to external spins, in dealing with a N- V ensemble the resulting dynamics will be governed by average N- V properties [31]. It is not immediately clear, therefore, whether previous successful single N- V results are easily extendible to higher N- V densities.

In this work, we present an experimental study into the challenges associated with the scaling up of previous single N- V results [10–12] to shallow N- V ensembles, with the goal of demonstrating polarization transfer compatible with the vision of Ref. [20]. We investigate the polarization dynamics over a range of parameters using a robust, pulse-based scheme (PulsePol [18]). Starting with an ideal room-temperature scenario, we polarize a solid target (biphenyl) and analyze our results using a theoretical model. In doing so, we experimentally determine an upper bound on the polarization (or cooling) rate in the current “best-case” scenario and discuss the implications of this. We then probe the extent to which the addition of molecular diffusion compromises the polarization transfer by repeating experiments using fluid targets of varying

viscosities. We conclude with a discussion of the results and an assessment of the prospects for future work.

II. RESULTS

A. Polarizing a solid target

We first investigate the interaction between our shallow N- V ensemble and hydrogen spins within a solid target. All experiments are carried out over a $50 \times 50 \mu\text{m}^2$ field of view (FOV) using a widefield N- V microscope. Elements of this setup are depicted schematically in Fig. 1, including a 532 nm laser for N- V state initialization and readout, and a microwave (MW) resonator for spin state

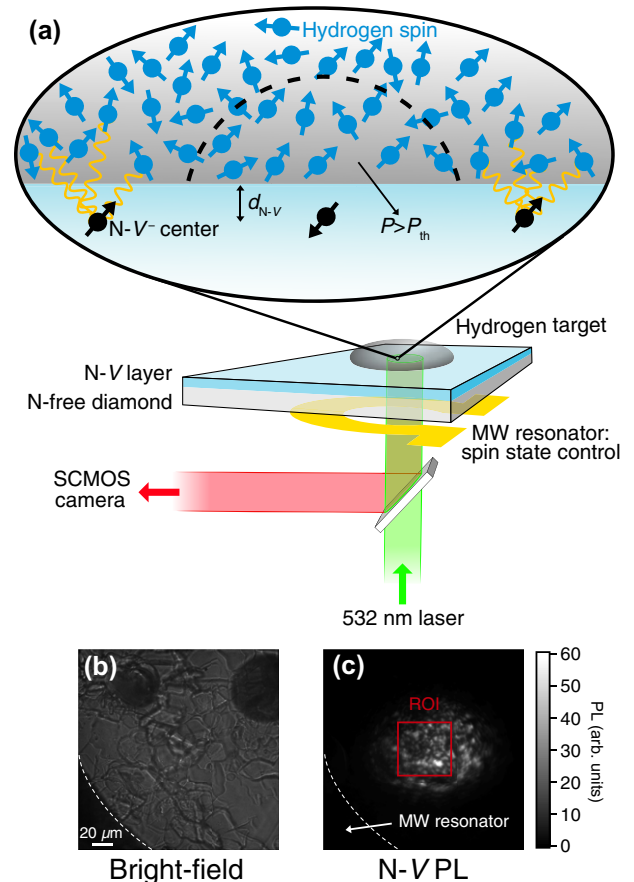


FIG. 1. (a) Schematic of the experimental setup, depicting widefield N- V microscope and polarization transfer via dipolar coupling between an ensemble of N- V centers at a depth d_{N-V} below the diamond surface and a number of nearby nuclear spins. Polarization P greater than the thermal background (P_{th}) is built up locally to a N- V (dashed semicircle) as its spin polarization (quantized along external bias field B) is donated to the nuclear bath, before spin diffusion spreads this polarization into the bulk target. (b) Bright-field image of a $200 \times 200 \mu\text{m}^2$ region, showing biphenyl crystals on the diamond surface. (c) N- V photoluminescence (PL) image of the same region in (b), with the $50 \times 50 \mu\text{m}^2$ region of interest (ROI) used for this work marked by the red square.

control (see Appendix A for details). The FOV is denoted by the red square in the N- V PL image, chosen to coincide with a region of relative laser intensity and MW driving uniformity. Biphenyl crystals are formed on the surface of the diamond and encapsulated with epoxy to prevent subsequent sublimation (details in Appendix B). As our experiment addresses a large number of N- V centers simultaneously and about a $100 \mu\text{m}^3$ target volume, it can be considered as a “toy model” for a realistic, NMR-relevant implementation of the technique. Achieving polarization over this scale presents two principal challenges: the technical, experimental challenge of successfully addressing a large number of N- V centers over a useful field of view, and the material problem of reduced coherence times for high-density N- V ensembles. The PulsePol pulse sequence has been identified as the best currently accessible approach in addressing these concerns due to its robustness to realistic experimental errors (see Appendix C) [18]. Its action as a decoupling sequence is also beneficial in addressing our ensembles as they are subject to broadband noise from the nitrogen spin bath and surface defects. The ensembles are created using a 2.5 keV ^{15}N implant with a fluence of $(1-2) \times 10^{13} \text{ cm}^{-2}$ and a 1100 °C ramped anneal, leading to N- V centers lying within 10 nm of the surface with an areal density $\sigma_{\text{N-}V} \approx 1500 \mu\text{m}^{-2}$ (see Appendix B for details). Coherence times in excess of 10 μs are achieved using PulsePol, which is a considerable extension over low-order decoupling sequences in this regime [24,31].

The PulsePol pulse sequence, depicted in Fig. 2(a), sets an average Hamiltonian that approximates a flip-flop Hamiltonian between the N- V and a target nuclear spin species when a resonant condition $\tau_{\text{res}} \approx n\tau_L/2$ for odd integer n is met, where τ is defined as the duration of the unit sequence, repeated $2N$ times, and τ_L is the target Larmor period. Note that the equality is only approximate as the resonant condition may be shifted by the accumulation of phase errors without degrading the strength of the interaction [18], so in practice τ_{res} is found experimentally.

Figure 2(b) shows a typical PulsePol spectrum obtained by sweeping τ for fixed $N = 30$. The y axis is the normalized N- V PL averaged over the full FOV, which is a proxy for the population of the $m_s = 0$ N- V spin state, referred to as N- V spin polarization in what follows. The dip at $\tau \approx 840$ ns is the $n = 3$ hydrogen resonance, which produces the strongest interaction [18] and will be the focus of this work. When the resonant condition is met, a large drop in N- V spin polarization is observed, which is inferred to have been symmetrically donated to the target hydrogen bath by virtue of the PulsePol sequence design [18]. To gain an insight into the dynamics of the apparent polarization transfer, we examine the decay of N- V spin polarization versus total interaction time $t = 2N\tau$ by increasing N for fixed τ , and compare the resonant ($\tau = \tau_{\text{res}}$) case with the off-resonant case. Both sets of data are shown in Fig. 2(c), where the red points are estimates of the off-resonance

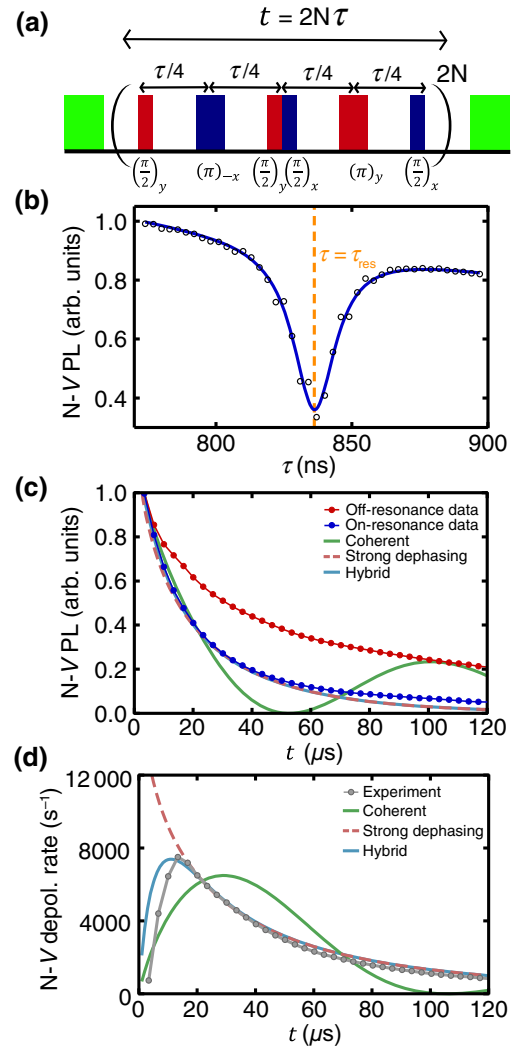


FIG. 2. (a) Schematic of the PulsePol pulse sequence. (b) An $N = 30$ PulsePol spectrum scanning τ , with $T_{2,n}^*$ -limited hydrogen resonance visible at $\tau = 840$ ns. The solid blue line is a fit to the data (black circles) using a Lorentzian lineshape. (c) Off- (red) and on-resonance (dark blue) N- V decay with PulsePol sequences of increasing length and total duration $t = 2N\tau$. Solid lines give theoretical predictions based on numerically integrated values of A_0 , and Γ_2^{tot} for the coherent (green), strong-dephasing (light red), and hybrid (light blue) cases. Data normalized to the maximum N- V spin contrast. (d) Experimentally determined N- V depolarization rate (gray circles) and comparison to theory (solid curves).

decay at $\tau = \tau_{\text{res}}$ made by averaging data obtained at $\tau = \tau_{\text{res}} \pm 60$ ns, and the blue points show the resonant decay. Following the treatment of Refs. [10,23,32], we represent the resonant decay curve as a product of the background N- V decoherence (which is independent of any polarization dynamics) and the resonant contribution,

$$P_{\text{N-}V}(t) = P_{\text{off}}(t)P_{\text{res}}(t), \quad (1)$$

where $P_{\text{N-}V}$ is the population of the N- V $m_s = 0$ spin state (assumed to be perfectly initialized at $t = 0$).

For the present experiment, we find that the off-resonance decay is well fit by $P_{\text{off}}(t) = \exp[-(t/T_2^{\text{N-V}})^\beta]$ with $T_2^{\text{N-V}} = 22 \mu\text{s}$ and $\beta = 0.42$. In analyzing the shape of the resonant decay curve, it is useful to consider the extreme cases of the strong and negligible dephasing regimes. In both cases, we assume that there is a direct correspondence between extra coherence lost by the N- V when the resonant condition is met and that resulting from the flip-flop interaction in the effective Hamiltonian.

In the ideal case, there is coherent coupling between N- V and the hydrogen spin bath, and the evolution of the system is governed by

$$P_{\text{res}}(t) = \cos^2\left(\frac{A_0 t}{2}\right), \quad (2)$$

where $A_0 = \sqrt{\sum_j A_j^2}$ is the summed dipolar coupling between the N- V and full spin bath, made up of j hydrogen spins [10,23]. In the absence of decoherence, the flip-flop time $\tau_0 = \pi/A_0$ corresponds to the full donation of the N- V 's spin polarization to the target bath.

Conversely, in the strong-dephasing regime $\Gamma_2^{\text{tot}} \gg A_0$, where $\Gamma_2^{\text{tot}} = \Gamma_2^{\text{N-V}} + \Gamma_2^{\text{H}}$ (with $\Gamma_2^{\text{N-V}} = 1/T_2^{\text{N-V}}$ and Γ_2^{H} the hydrogen spin dephasing rate) is the total dephasing rate of the system under the PulsePol sequence, incoherent polarization transfer proceeds via the monotonic evolution [10,23]

$$P_{\text{res}}(t) = \exp\left(-\frac{A_0^2}{\Gamma_2^{\text{tot}}} t\right). \quad (3)$$

With an average N- V depth measured at $d_{\text{N-V}} \approx 6 \text{ nm}$ (see Appendix B for details), we expect our experiment to fall primarily in the strong-dephasing regime [23].

Figure 2(c) shows the extremal cases as predicted by numerical integration of the quantities A_0 and Γ_2^{tot} (which is affected by a nuclear dephasing gradient due to the presence of unpaired electron spins on the diamond surface [23]; see Appendix D) with $d_{\text{N-V}} = 6 \text{ nm}$. Good agreement is found with the strong-dephasing case, indicating that Eq. (3) gives a good approximation to the polarization dynamics in our experiment. It is possible, however, that there are some target spins that exist in or near the strong coupling ($A_0 > \Gamma_2^{\text{tot}}$) regime, implying the existence of a small coherent component in our data. In order to capture this interchange between coherent and incoherent behavior, as averaged over our measurement ensemble, we introduce the following phenomenological adjustment to Eq. (3):

$$P_{\text{N-V}}(t) = \exp[-(\Gamma_2^{\text{N-V}} t)^\beta] \left\{ \exp(-\Gamma_{\text{int}} t) \cos^2\left(\frac{A_0 t}{2}\right) + [1 - \exp(-\Gamma_{\text{int}} t)] \exp\left(-\frac{A_0^2}{\Gamma_2^{\text{tot}}} t\right) \right\}. \quad (4)$$

Here Γ_{int} is a parameter controlling this interchange. Setting $\Gamma_{\text{int}} \approx \Gamma_2^{\text{tot}} \approx 100 \text{ kHz}$ makes only a subtle adjustment to the decay shape; however, the influence of this factor becomes more apparent in Fig. 2(d). Here, we plot the difference between the experimental off- and on-resonance data, normalized by the difference in PL given by ensembles initialized in the $m_s = 0$ and $m_s = -1$ spin states (representing maximal N- V coherence), and divided by t at each point. This amounts to a direct experimental measurement of the rate of additional N- V depolarization due to the interaction with the hydrogen bath, which we infer to correspond directly with the hydrogen cooling rate, defining

$$u(t) = \frac{1}{t} [P_{\text{off}}(t) - P_{\text{N-V}}(t)], \quad (5)$$

which is a generalization of the definition in Refs. [20,23]. Note that this equation is exact when the hydrogen bath polarization is given by $P_{\text{H}}(t) = P_{\text{off}}(t) - P_{\text{N-V}}(t)$ and an overestimate when there is additional resonant coherence loss that does not contribute to useful polarization. The current experiment is unable to make the distinction and so the cooling rates quoted in this work represent upper limits of the true values.

The experimental data peaks at a value of $u \approx 7500 \text{ s}^{-1}$ for $N = 8$, corresponding to an interaction time $t \approx 13 \mu\text{s}$. The strong-dephasing approximation vastly overestimates the N- V depolarization rate for small times because it sees coherence decrease exponentially while coherent transfer is sinusoidal ($\sin^2 x \approx x^2$ for small x), while the fully coherent case predicts an accurate maximum depolarization rate but for a much longer sequence than the actual $N = 8$. The modification of Eq. (4) is required to give qualitative agreement with the data, producing a peak positioned according to the value of Γ_{int} . The good agreement we find with a model that contains only experimentally determined parameters and one free parameter Γ_{int} suggests that the assumption that N- V depolarization corresponds to hydrogen bath polarization is valid. Additionally, the close correspondence between the magnitude of the maximum experimental cooling rate and that predicted in the coherent case (accounting for background N- V decay) supports the use of the coherent model for general predictions as in Ref. [20].

Under continuous application of this optimal sequence, polarization can be built up within the target bath according to the differential equation

$$\frac{\partial P(\mathbf{R}, T)}{\partial T} = u(\mathbf{R})[1 - P(\mathbf{R}, T)] - \Gamma_{1,n} P(\mathbf{R}, T) + D_n \nabla^2 P(\mathbf{R}, T), \quad (6)$$

where $\Gamma_{1,n}$ is the nuclear relaxation rate, D_n is the nuclear diffusion constant, and $u(\mathbf{R})$ is the position-dependent

cooling rate, integrating to the maximum experimentally determined N- V depolarization rate [20]. Approximating the hydrogen spin diffusion in the biphenyl crystal to that of a spin-1/2 species on a cubic lattice, $D_n \approx 0.22(\mu_0/4\pi)\hbar\gamma_n^2\rho_n^{1/3}$ [33], we find that $D_n \approx 571 \text{ nm}^2/\text{s}$. Thus, diffusion out of the N- V sensing volume will happen on a comparable timescale to the polarization transfer, leading to efficient polarization of the total bath but only a small buildup of polarization local to the N- V . This is not a problem for the ultimate implementation of the technique, but it does make unambiguously measuring polarization buildup using the same shallow N- V centers difficult.

Figure 3 shows an attempt to evidence polarization buildup within the N- V sensing volume using the optimal sequence previously identified ($N = 8$). This measurement is made as per the pulse sequence schematic in Fig. 3(a): a resonant PulsePol sequence is repeated for a time $t_{\text{pol}} > T_{1,n}$ and polarization buildup measured through the change in N- V PL. The procedure is then repeated with the N- V initialized in the $m_s = -1$ spin state to reset the nuclear bath. Here we utilize the fact that, by design, the PulsePol sequence only interacts with one spin state (e.g., $|\downarrow\rangle$) and polarizes the coupled spins into the other (e.g., $|\uparrow\rangle$) [18]. Therefore, as the net polarization builds up according to Eq. (6), there will be a small effective reduction in A_0 due to the changing state populations within the N- V

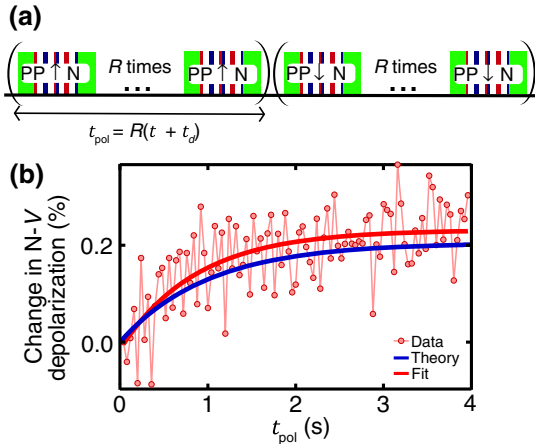


FIG. 3. (a) Pulse sequence used to demonstrate local polarization buildup: a resonant PulsePol sequence (PP \uparrow) of length N is repeated R times to reach a steady state. The bath is then reset with a “depolarization” sequence of the same length, where polarization in the opposite direction is achieved by initializing the N- V in the $m_s = -1$ spin state prior to applying each PulsePol sequence (i.e., PP \downarrow). (b) Measured polarization buildup within the N- V sensing volume following repeated application of the PulsePol sequence previously identified to give the maximum cooling rate ($N = 8$). The blue line is the theoretical prediction based on the solution of differential equation (6) with $T_{1,n} = 1$ s and the red line is a fit to the experimental data, finding $T_{1,n} \approx 0.88$ s.

sensing volume. This change is read out as an increase in N- V PL corresponding to reducing the PulsePol resonance depth.

The solid blue curve in Fig. 3(b) is a theoretical prediction obtained by solving Eq. (6) using the experimentally determined $u = 7506 \text{ s}^{-1}$ and setting $T_{1,n} = 1/\Gamma_{1,n} = 1$ s. Here $T_{1,n}$ sets the timescale to reach the steady state (we use a simple exponential rise with time constant $T_{1,n}$). Higher values of $T_{1,n}$ will allow higher levels of polarization to accumulate, but this will result in only a modest increase in the steady-state value as we make a local measurement and D_n is large compared to u . Biphenyl $T_{1,n}$ has been reported to be as high as approximately 10 min at room temperature and approximately 2 T [34], but it is likely to be much shorter at our field (about 430 G). The steady-state PulsePol dip reduction (the expected measurement contrast) for a N- V 6 nm from the surface is calculated by numerically integrating over the steady-state probability distribution. The predicted contrast change is extremely small (approximately 0.2%) despite a significant overall polarization of 1800 equivalent hydrogen spins per N- V due to the role of spin diffusion in driving polarization out of the N- V sensing volume.

The experimental data (pink circles) are consistent with the theory, but the signal is within noise. Each data point in Fig. 3(b) is the difference in PL obtained between “signal” and “reference” camera exposures (that differ by a π pulse prior to readout to account for common mode noise) and thus represents the cumulative PL given by $R \approx 2000$ repetitions of the PulsePol sequence. The signal-to-noise ratio is small as measurement times are necessarily long (hours to days), over which time additional noise from magnetic field and temperature shifts are difficult to control. Compounding this is the long laser pulse duration used ($30 \mu\text{s}$), necessary to ensure maximal and even ensemble initialization across the full FOV but reducing the spin readout contrast. This also reduces the polarization duty cycle in the steady-state polarization produced, taking $u \mapsto u(t_{\text{seq}})[t_{\text{seq}}/(t_{\text{seq}} + t_d)]\mathcal{F}$, where t_{seq} is the optimal sequence length and t_d is the sequence “dead time,” exceeding $30 \mu\text{s}$ in this case, and a finite initialization fidelity $\mathcal{F} = 0.8$ has been included. A higher laser power density would address this issue and measuring polarization buildup is thus expected to be easier on a confocal microscopy system, where the laser is focused to a diffraction-limited spot. However, the lower power density in our experiment is necessary to access a wide field of view. Fortunately, this is a technical requirement that could be overcome in a realistic implementation by simply using an appropriate high-intensity pumping source and thus it is possible for t_d to be negligible. The solid red curve in Fig. 3(b) is a fit to the experimental data (again a single exponential rise), yielding a similar total contrast change on the slightly shorter timescale $T_{1,n} \approx 0.9$ s.

An alternative scheme to detect local polarization involves pulsing the nuclear ensemble with a resonant $\pi/2$ pulse. This induces an ac field due to the spins' Larmor precession that is stronger than the statistical polarization signal, which can then be read out using the N- V ac magnetometry. This has the advantage of separating the polarization and readout processes and may produce a measurable signal even though the local polarization is not expected to be sufficient to produce a signal-to-noise ratio enhancement compared to the continuous acquisition of statistical polarization [20]. However, this will still be a small signal with predicted strength similar to that read out using the polarization sequence (i.e., the net polarization enhancement generated within the N- V sensing volume will not greatly exceed the statistical polarization), so we do not expect that this would achieve a dramatically improved result. Conducting N- V NMR in this manner using a deeper N- V ensemble to access a larger sensing volume and allow for the detection of the full polarization generated [20–22] is, however, beyond the scope of the current work.

B. Polarization transfer scaling with N- V T_2

Having demonstrated and analyzed polarization transfer in a current best-case scenario, we now further probe the dependencies of Eq. (4) by varying the N- V and target properties. To see this clearly, we remove the influence of the background N- V decay as much as possible by, for every data point, dividing the difference between the on- and off-resonance measurements by the off-resonance value at that point, to obtain a normalized polarization signal $S(t) \equiv P_H(t)/P_{\text{off}}(t)$. Taking our earlier definitions and Eq. (4) we find that

$$S(t) = 1 - \exp(-\Gamma_{\text{int}}t) \cos^2\left(\frac{A_0 t}{2}\right) - [1 - \exp(-\Gamma_{\text{int}}t)] \exp\left(-\frac{A_0^2 t}{\Gamma_2^{\text{tot}}}\right), \quad (7)$$

so that we have an exponential rise to unity with the possible appearance of sinusoidal behavior at short times. Although we consistently observe saturation to a value below one due to the increased influence of decoherence at long times, this equation well describes our data for times $\leq 120 \mu\text{s}$, which is well beyond a realistic optimal sequence length of approximately $10 \mu\text{s}$.

First we examine the influence of N- V T_2 , which still enters into Eq. (7) through the previous definition of Γ_2^{tot} . In Fig. 4 we present the normalized polarization transfer signal obtained for two solid hydrogen targets, biphenyl and poly(methyl methacrylate) (PMMA), and using two diamond samples with different T_2 —varying between approximately 7 and 22 μs (with minimal variation in the exponent β), as shown in the off-resonance PulsePol decay curves in Fig. 4(a). The T_2 value changes

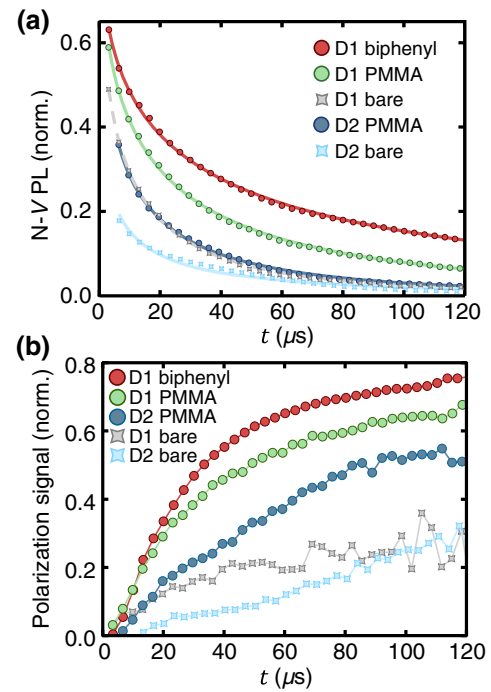


FIG. 4. (a) Comparison of background (off-resonance) PulsePol T_2 decay for different solid targets (biphenyl, PMMA, bare diamond surface) and diamond samples (labeled D1 and D2). Solid lines are fits to an exponential decay $\exp[-(t/T_2^{\text{N-V}})^\beta]$ with β ranging from 0.42 to 0.47. Data normalized to the maximum N- V spin contrast for a given diamond. (b) Normalized polarization transfer for different solid targets and bare diamond hydrogen signals for two diamond samples.

between two diamonds, D1 and D2, as D2 is implanted with twice the dose of ^{15}N ions as D1 and so features a more dense nitrogen spin bath and possibly more implantation-induced crystal damage (see Appendix B for diamond sample details). Additionally, however, T_2 is also found to vary based on the hydrogen target present on the diamond surface. This effect was confirmed to be a genuine background effect (rather than off-resonant polarization transfer) by the appearance of similar variation in Hahn echo T_2 (see Appendix C) and has previously been explained in terms of an electronic passivation of surface electron density [35].

This shows that, even where the nitrogen spin bath is expected to be the dominant source of N- V decoherence as in our samples, unpaired electron spins on the diamond surface (or other surface effects) are also significant. The dielectric properties of PMMA and biphenyl are unlikely to explain such a large difference, but a similar electrical passivation may be possible through a separate mechanism such as chemisorption to unpaired electron spins on the surface through, for example, a target double bond [36,37]. Regardless, the source of this effect is not important for the current discussion, though it conveniently allows us to

probe the dependence of the polarization dynamics on $N-V T_2$ in a controlled way.

The effect of the target-specific $N-V T_2$ is evident through comparison of the D1 biphenyl and D1 PMMA curves in Fig. 4(b). Polarization transfer to biphenyl is observed to be more efficient than to PMMA, despite PMMA's greater hydrogen density ($\rho_{\text{H}}^{\text{PMMA}} = 56 \text{ nm}^{-3}$ versus $\rho_{\text{H}}^{\text{biph}} = 41 \text{ nm}^{-3}$) and negligible differences in $T_{2,\text{H}}^*$ ($= 1/\Gamma_2^{\text{H}}$ for a solid target) for both targets as measured via XY8 correlation spectroscopy [38]. The difference in $N-V T_2$ is sufficient to explain our data and is most evident at longer times when the system's evolution is well described by the strong-dephasing limit. For short times (less than 10 μs), when coherent evolution is prevalent, PMMA gives a stronger signal than biphenyl as the coherent polarization exchange is related only to the coupling strength $A_0 \propto \sqrt{\rho_{\text{H}}}$.

Comparing the PMMA signal from the two diamonds, it is clear that a reduction in $N-V T_2$ reduces per- $N-V$ polarization transfer efficiency (possibly small differences in coupling strength too due to depth distribution; see Appendix B). This results in a 3.5-fold reduction in the maximal experimentally measured per- $N-V$ cooling rate. This is greater than the difference in estimated $N-V$ density between the two samples, although there is room to improve the properties of high-density $N-V$ ensembles (see Sec. III). A similar difference is also observed in the respective bare diamond signals, which is believed to arise from an adventitious hydrogen layer on the diamond surface [38,39]. This signal is expected to be present in all our data as it is not removed by any cleaning process. We do not subtract it from the data in this work as in principle any polarization transferred to this layer can diffuse into the target and, regardless, its contribution to the maximum cooling rates for solid targets is small.

C. Effect of target diffusion

The results of Sec. II B demonstrate the impact of changing Γ_2^{tot} through varying $N-V T_2$. Differences in the target T_2 will affect polarization transfer in the same way. While the measured $T_{2,\text{H}}^*$ values for the two solid targets compared are similar, molecular diffusion of target spins into and out of the $N-V$ sensing volume during the polarization transfer will result in a loss of phase coherence in the interaction (and thus an effective T_2 , scaling as D_n^{-1}). When using a pulse-based scheme such as PulsePol, this is compounded by an additional loss in polarization transfer efficiency, as the requirement for the $N-V$ -target interaction to be long enough lived for the average Hamiltonian to accurately approximate a flip-flop Hamiltonian introduces an effective reduction in coupling that scales as D_n^{-2} when the diffusion timescale exceeds the Larmor period [23]. We therefore expect the cooling rate $u_{\text{max}} \propto A_0^2/\Gamma_2^{\text{tot}}$ using PulsePol to scale as D_n^{-3} for fluid targets.

This represents a challenge for genuine liquid-state hyperpolarization, which is an attractive niche for $N-V$ -based techniques to fill as current liquid hyperpolarization techniques are less efficient than their solid-state counterparts [40]. Additionally, $N-V$ -based micron-scale NMR has recently emerged as having utility for analysis of liquid samples [21,22], and has recently been successfully integrated with Overhauser DNP and parahydrogen-based hyperpolarization techniques [41,42]. It has been proposed that an all-diamond hyperpolarization and NMR platform could be competitive in this regime [20]. The goal of this section, then, is to experimentally determine the efficiency of polarization transfer to targets in the liquid state compared to those in the solid state, with diamond material properties held constant.

To assess the impact of molecular diffusion on polarization transfer, several mixtures of glycerol and water are produced with the glycerol volume fraction χ_g ranging from 0 (pure water) to 1 (pure glycerol). Assuming that the static coupling between bath hydrogen spins and $N-V$ is constant (justifiable as ρ_{H} should vary by less than 1% under laboratory conditions [43]) and any effect of changing background $N-V$ decoherence due to target dielectric properties is minimal (see Appendix E: $N-V T_2$ changes minimally), any loss in polarization transfer efficiency with reduced viscosity can be ascribed to the changing molecular dynamics.

In Fig. 5(a) we plot the inferred polarization transfer, with the background $N-V$ decay (diamond D1) normalized out for clarity. A clear trend is visible, with the growth of the pure glycerol resonance comparable to a solid target due to its high viscosity, while diluting with water down to $\chi_g = 0.5$ gives reduced but still measurable polarization transfer. Using pure water as a target, on the other hand, gives no measurable increase in signal over the bare diamond hydrogen resonance. We also include a measurement obtained using diamond D2 and a pure glycerol target for comparison with the effect of changing $N-V T_2$, which is consistent with the results of the previous section.

In Fig. 5(b) we plot the $N-V$ depolarization rates (which we again take to correspond to the cooling rate) as in Sec. II A. Compared to the biphenyl results, the maximum cooling rate for pure glycerol is roughly a factor of 2 lower, despite almost identical background $N-V T_2$. XY8 correlation spectroscopy measures only a small reduction in target T_2 that is not enough to explain the full reduction, especially when considering that glycerol is more hydrogen-dense than biphenyl ($\rho_{\text{H}}^{\text{gly}} \approx 65 \text{ nm}^{-3}$). Thus, our data support an additional reduction in polarization transfer as a result of using the PulsePol sequence: assuming again that the maximum experimental cooling rate is proportional to the theoretical strong-dephasing limited rate, this result suggests a reduction in effective coupling strength by a factor of approximately 3. However, Fig. 5(b) shows that reducing $N-V T_2$ by using D2 instead of D1

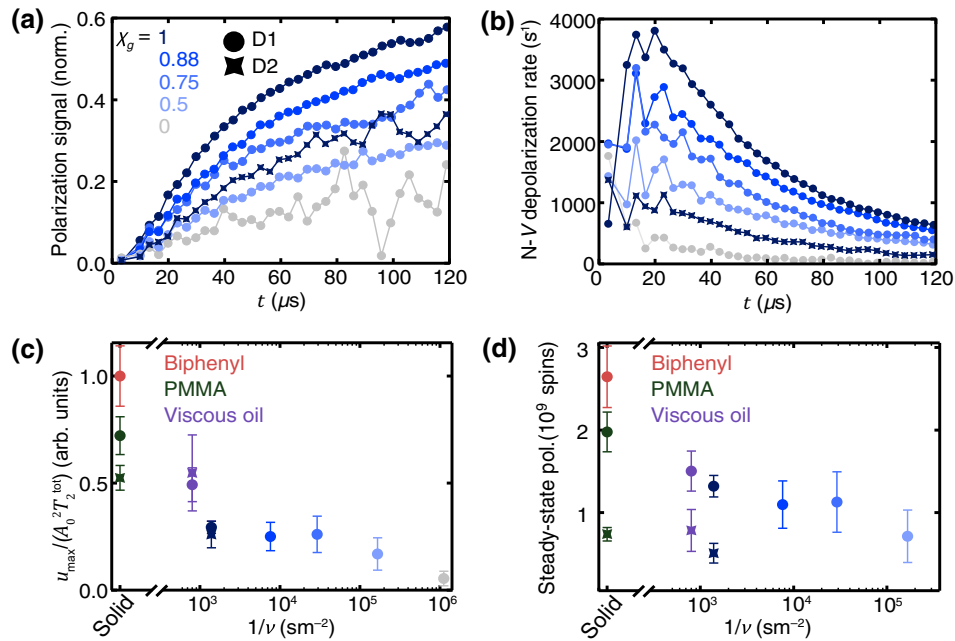


FIG. 5. (a) N - V polarization transfer to glycerol-water mixtures of various compositions denoted by the glycerol volume fraction χ_g , normalized to background decoherence. Data obtained with diamond D2 (stars) and $\chi_g = 1$ also shown. (b) Experimental cooling rates from the data in (a). (c) Plot of maximum cooling rate, normalized with respect to the theoretical no-diffusion value, against the inverse of the kinematic viscosities of the glycerol mixtures and additional liquid- and solid-state targets for comparison. Error bars extrapolated from the range of cooling rates obtained within $N = N_{\text{opt}} \pm 2$, where N_{opt} corresponds to the maximum cooling rate. (d) Steady-state nuclear polarization values predicted by a simulation using the measured cooling rates, N - V densities, and the addressed field of view of $50 \times 50 \mu\text{m}^2$. Idealized parameters are used, including $\mathcal{F} = 0.8$, $t_d = 0 \mu\text{s}$, and $T_{1,n} = 1 \text{ s}$.

made a larger difference than diluting glycerol by 50% by volume in water, which is expected to result in an increase in D_n of over an order of magnitude [44].

Figure 5(c) summarizes the cooling rate results for the glycerol mixtures and other targets for comparison. As well as the solid targets already discussed, we also include results obtained with a highly viscous oil (Sigma-Aldrich 1250 cSt I0890 immersion oil). As a figure of merit, we divide the maximum measured cooling rate by the theoretical strong-dephasing cooling rate for each data point, normalizing to the maximum value obtained (biphenyl). In doing so, we normalize out any differences due to T_2^{tot} , d_{N-V} , or ρ_H , isolating the effective coupling reduction due to molecular diffusion [23]. Again, we include data obtained with diamond D2 as well as D1 for three of the targets, finding that differences between the diamonds are well normalized out, providing further support for the model.

This quantity is plotted against the inverse of the kinematic viscosity, a readily available quantity that is proportional to D_n through the Stokes-Einstein equation (although this proportionality will not necessarily be identical for all targets). The remaining trend confirms that increasing molecular diffusion makes polarization transfer to liquid targets less efficient than to solid targets using PulsePol. However, the dependence in the

intermediate viscosity regime (for glycerol series, $\chi_g = 0.5$ – 1) is weaker than expected.

This is also true for the variation of measured T_2^H ($= 1/\Gamma_2^H$ for a fluid target) for the series of glycerol mixtures, where a reduction is present but with weaker scaling than the expected D_n^{-1} . Within error, our data are consistent with either variation in D_n of only approximately 20% between $\chi_g = 1$ and $\chi_g = 0.5$, or with the full series exhibiting characteristic diffusion times less than the hydrogen Larmor period (approximately 550 ns) (see Appendix E). In both cases this contradicts expectation [44]. However, the discrepancy may be explained either in terms of a near-surface adsorption layer where fluid motion is not well described by bulk viscosity values, or possible near-surface solidification, both of which have previously been suggested [35,38].

In Fig. 5(d) we plot the total steady-state nuclear polarization predicted to be produced by the maximum experimentally determined cooling rates and taking into account the measured σ_{N-V} for the respective samples ($\sigma_{N-V} = 1400 \mu\text{m}^{-2}$ for D1 and $1800 \mu\text{m}^{-2}$ for D2) and the area addressed ($50 \times 50 \mu\text{m}^2$). As diffusion drives polarization away from the N - V sensing volume as in Sec. II A in all cases, local saturation effects are negligible and the simulated steady-state hydrogen polarization per N - V tends towards $u(t_{\text{seq}})[t_{\text{seq}}/(t_{\text{seq}} + t_d)]\mathcal{F}$ with $T_{1,n} = 1 \text{ s}$. Here we

plot the limiting case of $t_d = 0$. As these data are not normalized against $A_0^2 / \Gamma_2^{\text{tot}}$, the effect of N- V T_2 can again be seen here, with the slight increase in N- V density in D2 insufficient to offset the reduction in T_2 in this sample.

These results confirm the difficulty of achieving polarization to highly fluid targets, with no evidence found for significant interaction with water. However, in the intermediate viscosity region, the observed dependence is weaker than theoretically predicted. Sufficiently viscous liquids diffuse slowly enough to interact with strength within a factor of 2 of that of solid targets and so in this regime N- V -based hyperpolarization appears to hold promise. This could be applicable to micron-scale N- V NMR modalities and hyperpolarization of more fluid targets could be achievable by exploiting the variation of viscosity with temperature; polarizing a slow-moving liquid at low temperature and then heating up, similar to a freeze-thaw cycle commonly used for solution-state DNP but without the need for a convenient phase transition. Additionally, the apparent reduction in molecular diffusion near the diamond surface could be exploited to achieve greater polarization transfer than would be expected for a fluid with true bulk properties. Although this effect requires more rigorous characterization, it is likely that it is confined to within a few nanometers of the diamond surface and so molecular and/or spin diffusion will quickly take polarization into the bulk fluid.

III. DISCUSSION

Our results show that the coherence properties in current dense, shallow N- V ensembles are sufficient to transfer a significant amount of polarization to an external nuclear spin bath, in both solids and sufficiently viscous liquids. The PulsePol protocol is successful in allowing the use of approximately 10^6 N- V centers in parallel and the extension of the current experiment to an even larger active area is feasible provided technical challenges of microwave delivery and high-intensity laser illumination are met over that area. A higher-intensity source for the N- V optical pumping could allow a significant decrease in the laser pulse duration used, resulting in an improved polarization duty cycle that would provide an improvement in the steady-state hydrogen polarization over the current experiment.

In the limiting case of achieving perfect N- V initialization instantly, the cooling rate demonstrated with biphenyl is sufficient to generate an average polarization of $P = 2.7 \times 10^{-4}$ within the $1\text{-}\mu\text{m}$ -thick layer closest to the diamond (taking the uniform N- V density $\sigma_{\text{N-}V} = 1400 \mu\text{m}^{-2}$ and $T_{1,n} = 1$ s). This represents an over 3 orders of magnitude enhancement over the Boltzmann polarization under our laboratory conditions, owing mainly to the low magnetic field used (about 430 G) and operation at room temperature. The absolute polarization is small, however,

and would not scale with magnetic field or temperature where a brute-force Boltzmann polarization enhancement could be obtained. Furthermore, practical realization of this technique for bulk NMR enhancement would require structuring a diamond polarization cell such that the volume above the diamond slab is of a micron scale or smaller, which represents a significant engineering challenge [20]. However, there are also significant material improvements that can be made to enhance the polarization obtained.

The N- V yield in both diamond samples used in this study (1.4% for D1 and 0.9% for D2) is low compared to that of typical deeper ensembles [45] and it has been suggested that techniques such as Fermi engineering could enhance this yield towards 100% [46]. In the latter case, an improvement of nearly 2 orders of magnitude may be achievable in the area-normalized polarization generated, whereas even in the former case a factor of 2–5 improvement is possible. The difference between yields in shallow and deeper ensembles can be understood in terms of band bending due to imperfections in the oxygen-terminated diamond surface. Improving this is an active area of research; for example, there are current efforts to understand and control the diamond surface through optimized cleaning and annealing strategies [47].

Reducing near-surface band bending will also result in a shallower mean N- V depth, resulting in stronger coupling with the external spin bath and larger cooling rates (scaling with $d_{\text{N-}V}^{-3/2}$ in the coherent case and $d_{\text{N-}V}^{-3}$ in the strong-dephasing limit). The dependence shown in Sec. II B of N- V T_2 on hydrogen target also shows that, even with the high nitrogen densities of the samples used, surface spins contribute significantly to N- V decoherence. The combined action of reducing the mean ensemble depth to that of the expected ion implantation range of a 2.5 keV implant approximately 4 nm and increasing N- V T_2 to a nitrogen-limited value would, according to our theoretical model outlined in Sec. II A, result in an additional cooling rate enhancement of upwards of 4 times.

Control over the diamond surface also has a final benefit: unpaired surface electron spins also contribute to the dephasing of the hydrogen spins closest to the diamond [23]. We included this factor in the analysis of Sec. II A, taking a typical surface electron density of $\sigma_e = 0.1 \text{ nm}^{-2}$ [26,27] that reproduced our experimental results well. Numerical integration of the quantity $A(\mathbf{R})^2 / \Gamma_2^{\text{tot}}(\mathbf{R})$, the cooling rate in the strong-dephasing limit, shows that this electron density results in a 44% drop in the effective coupling between a N- V 6 nm from the surface and the hydrogen bath (for biphenyl, see Appendix D for details).

Considering all of the above factors, we estimate that a total improvement of up to 2 orders of magnitude is achievable with realistic diamond material advancements. This would be sufficient, following successful diamond nanostructuring and integration with a NMR

probe, to achieve significant enhancements over thermal polarization [20].

The results of Sec. II C confirm that N- V hyperpolarization of low-viscosity liquid targets is beyond current capabilities, but the cooling rates obtained for more viscous targets are within a factor 2–3 of the solids. The transfer appears to be aided by an effective reduction in molecular diffusion near the diamond surface, possibly due to surface dragging effects or local drying brought about by laser heating. This surprising result may be beneficial for polarization to fluids with moderate viscosity ($D_n \approx 10^{-11} \text{ m}^2 \text{ s}^{-1}$), whereby polarization can be transferred to regions of locally low diffusion and allowed to diffuse into the bulk fluid. Diffusion constants of this order of magnitude are typical in liquid crystal and lipid bilayer targets [48,49], which could be appealing targets for N- V -based polarization. In particular, if polarization transfer to these targets remains within an order of magnitude of solid targets as in our experiment, the improvements to the diamond materials discussed above could provide a realistic avenue towards hyperpolarized N- V -based micron-scale NMR [20]. Further work is required to fully characterize the near-surface fluid dynamics, however. We emphasize that we do not have a direct measurement of the diffusion constants of the targets used in our experiments (local or bulk) and so the interpretation of our current results can only be qualitative. In principle, however, the high sensitivity of the PulsePol protocol's effectiveness to molecular diffusion may be leveraged to study surface-modified diffusion processes.

IV. CONCLUSION

We present an experimental study of polarization transfer from a N- V ensemble to an external nuclear target. We demonstrate evidence of polarization transfer in the closest to ideal case, to hydrogen nuclei within a solid target, finding agreement between experiment and an analytical model combining coherent and incoherent transfer mechanisms. We find that the polarization rate obtainable with current materials and with realistic experimental conditions is sufficient to achieve a modest (3 orders of magnitude over room-temperature, low-field Boltzmann conditions) enhancement over thermal polarization levels although spin diffusion prohibits direct detection within the N- V sensing volume. Still, this result is compatible with the vision of achieving meaningful NMR enhancement with a shallow N- V ensemble following realistic diamond material improvements.

Polarization of nuclear targets within the liquid state proved to be more challenging due to the theoretically predicted reduction in effective dipolar coupling strength inherent to this technique in the presence of molecular diffusion. However, although polarization of highly diffusive liquids (e.g., water) is unrealistic, our results

show polarization transfer efficiency to more viscous fluids within an order of magnitude of that to solid targets. This is a promising result that could mean N- V -based liquid-state hyperpolarization is viable following successful incorporation of a diamond hyperpolarizer with a liquid NMR probe. Other methods of polarization transfer such as lab frame cross relaxation are expected to perform better than PulsePol in the fluid target regime [23], although this protocol faces other challenges such as poor initialization fidelity \mathcal{F} at the resonance condition [50].

Considering the above points, the single largest driver of improved future prospects for N- V -based NMR enhancement will be centered around improving diamond material properties, particularly regarding the diamond surface. Our characterization of the diamond samples used in this study suggests that near-perfect control of diamond surface chemistry could result in multiple orders of magnitude improvement in polarization transfer efficiency using the PulsePol sequence, as well as the possibility of using other protocols.

ACKNOWLEDGMENTS

We acknowledge support from the Australian Research Council (ARC) through Grants No. DE170100129, No. CE170100012, and No. DP190101506. A.J.H. and G.A.L.W. are supported by an Australian Government Research Training Program Scholarship. T.T. acknowledges the support of JSPS KAKENHI (Grants No. 20H02187 and No. 20H05661), JST CREST (JPMJ CR1773), and MEXT Q-LEAP (JPMXS0118068379).

APPENDIX A: EXPERIMENTAL DETAILS

All experiments are carried out on a purpose-built wide-field N- V microscope, elements of which are depicted schematically in Fig. 1 of the main text. A 532 nm laser with an incident intensity of approximately 300 mW is used to excite and initialize the spin states of the N- V ensembles. Red PL is emitted in a spin state-dependent manner by the N- V centers as they relax back to the ground state and imaged onto a scientific complementary metal oxide semiconductor camera (SCMOS). This setup allows for imaging of the N- V centers' behavior under a variety of experimental protocols over a maximum of $200 \times 200 \mu\text{m}^2$ field of view with a diffraction-limited spatial resolution of approximately 400 nm.

Quantum sensing and polarization-inducing protocols typically require the delivery of MW radiation to the N- V ensemble in order to manipulate its spin state. This is achieved in our setup via a gold ring-shaped resonator deposited on a glass coverslip onto which the diamond sample is mounted. The MW radiation is delivered using a Rhode & Schwartz SMBV100A signal generator IQ modulated by a Keysight P9336A arbitrary waveform generator with 1 ns time resolution. A PulseBlaster ESR-pro

card controls the timing of MW pulse sequences, laser pulses, and camera triggers with a time resolution of 2 ns. All experiments are conducted under a bias field of approximately 430 G aligned with one set of N- V axes.

The diamond samples used in this study are (100)-oriented electronic grade chemical vapour deposition (CVD) substrates purchased from Delaware Diamond Knives. A 1- μm -thick layer of isotopically enriched (99.95%) ^{12}C diamond is overgrown via microwave plasma-assisted CVD [51] to both limit spin noise and eliminate spurious harmonic signals due to ^{13}C spins in N- V NMR experiments [52]. The shallow N- V ensembles used for sensing and polarization are then created via a low-energy ^{15}N ion implantation procedure [2.5 keV, dose $(1\text{--}2) \times 10^{13} \text{ cm}^{-2}$, InnovIon] and annealed using a ramp sequence culminating at 1100 °C to maximize N- V yield and ensemble coherence properties [31]. Oxygen surface termination is achieved using a boiling mixture of sulfuric and nitric acid. The result is a high-density N- V ensemble with mean distance from the diamond surface of $d_{\text{N-}V} \approx 7$ nm (see Appendix B).

APPENDIX B: SAMPLE AND TARGET CHARACTERIZATION

Two diamond samples are used for this study, one featuring a 2.5 keV ^{15}N implant with a dose of $1 \times 10^{13} \text{ cm}^{-2}$ (sample D1) and the other a ^{15}N implant of the same energy but with a higher dose of $2 \times 10^{13} \text{ cm}^{-2}$ (sample D2). The N- V^- density of these samples is estimated by comparing their fluorescence as measured on a confocal microscope to that given by a single N- V (in a separate sample) and assuming that the measured PL is purely from the negative charge state. The estimated overall N to N- V^- conversion ratios in these samples are 1.4% (D1) and 0.9% (D2), lower than typical conversion rates in deeper ensembles that can exceed 5% [45].

Following the method of Ref. [54], we measure the depth distribution of the N- V ensembles in our samples. We fit the pairwise differences of 5–6 XY8- k spectra with k ranging from 32 to 256 to the signal given by a model N- V distribution. The N- V distribution is modeled as the product of a Gaussian fit to the expected N depth distribution as simulated using the stopping range in matter (SRIM) software package (mean 4.6 nm, width 3.0 nm) and a Sigmoid function $\{1 + \exp[-p_1(x - p_2)]\}^{-1}$ representing an effective cutoff in N- V^- charge stability due to band bending. The slope p_1 and position p_2 of the cutoff are allowed to vary in the fitting routine, as is a final parameter p_0 that multiplies the distribution to ensure normalization. The distributions obtained are likely not uniquely defined by only a small number of XY8 spectra and we only use approximate mean depths in our analysis in the main text. Using the simpler method [53] and obtaining a single mean depth is consistent with our approach provided that $k > 64$

and so would be sufficient for this work. However, it is useful to know that our N- V distribution is well described by a known implanted N distribution and band bending, and motivates further work in improving near-surface N- V yield through diamond surface engineering. The reduced overall N- V yield is largely explained by this cutoff, suggesting that the local N- V yield could be constant for depths greater than approximately 7 nm depending on the sample. N- V charge stability is known to depend on the local electron donor density as well as the Fermi level position, however, and it is also possible that N:N- V conversion is reduced close to the surface due to the surface acting as an efficient vacancy trap during annealing, so the task of optimizing near-surface N- V production is not trivial.

Example distributions are shown in Fig. 6 alongside the implanted nitrogen distribution predicted by a SRIM simulation. The fit distributions are consistent with there being a constant N- V^- yield (likely similar to that of deeper ensembles) for depths deeper than some sharp cutoff that is dependent on the surface properties of individual samples. For shallower depths than this cutoff, the N- V^0 charge state is expected to dominate. Here we see that sample D2 has a deeper cutoff than D1, matching the difference in conversion ratios estimated from the samples' PL in comparison to that given by a stable single N- V^- center. The difference could be due to the higher implantation dose used on D2 creating greater damage to the diamond surface and explains why less polarization transfer is measured with this sample (even accounting for the greater N density).

Most liquid hydrogen targets are simply deposited onto the surface of the diamond where they are observed to be stable for the duration of the experiments. A polydimethylsiloxane well and shorter total measurement times are used for the water experiment to prevent evaporation. PMMA is deposited on the diamond and then allowed to cure at room temperature prior to measurement. Biphenyl crystals are deposited by dissolving biphenyl powder (Sigma-Aldrich, 99.5% purity) in isopropanol and allowing this solution to dry on the diamond surface. To prevent degradation of the crystals, they are encased within water and UV-curing epoxy. The resulting crystals, visible in bright-field images such as Fig. 1(b), are observed to be stable for the duration of the experiments. Between measurements of different targets, diamonds are cleaned first using appropriate solvent (dichloromethane, acetone, or ethanol) and then in a boiling mixture of sulfuric and nitric acid to ensure a clean, oxygen-terminated surface. In each case the hydrogen signal is observed to return to the bare diamond baseline.

The correlation time τ_c of the target spin bath can be measured using XY8 correlation spectroscopy [38]. For the hydrogen spins in the solid samples, τ_c directly gives the nuclear dephasing time $T_{2,n}^*$ as molecular motion can be neglected. For the fluid targets, the opposite is true: τ_c is governed primarily by spatial diffusion. These measured

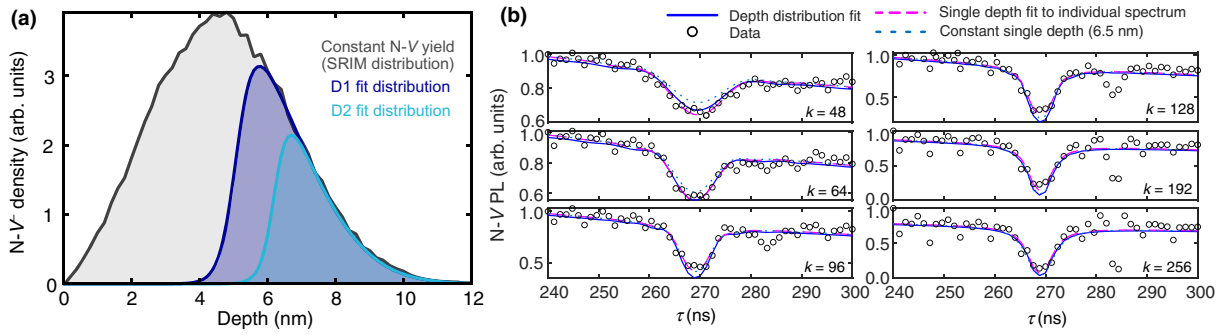


FIG. 6. (a) Comparison of fit N-V depth distributions for samples D1 (blue) and D2 (cyan) to simulated N implant distribution (gray, same for both samples up to a factor of 2). (b) Set of XY8- k spectra used to fit the depth distribution for sample D1, where k is the total number of π pulses used in the sequence. The signal reconstructed from the fit distribution (solid blue lines) gives good but not perfect agreement with the experimental data, indicating that a larger data set would be required to perfectly reconstruct the N-V depth distribution. Fitting directly to individual spectra using a single discrete depth as in Ref. [53] (dashed pink curves) results in a better fit to the data but a variable N-V depth depending on k . Using a constant discrete depth (dashed light blue curves), chosen to match the mean of the fit distribution (approximately 6.5 nm), provides reasonable agreement with the experiment except at low k . This indicates that, while knowledge of the full distribution is required to successfully reproduce the signal for all sequences, using the mean depth captures the main behavior, justifying the analytical approach used in the main text.

parameters are used in the theoretical calculations in the main text.

Figure 7 shows the variation of N-V T_2 with hydrogen target obtained using both off-resonance PulsePol

sequences (a) and the Hahn echo sequence (b). The T_2 scaling is similar in both cases, showing that the variation is due to a changing noise spectrum rather than polarization behavior.

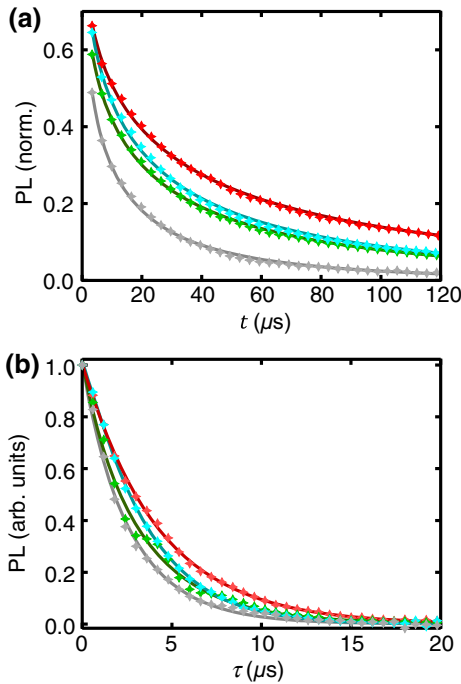


FIG. 7. (a) Off-resonance PulsePol decays with glycerol (red), viscous oil (blue), and PMMA (green) on the diamond surface compared to in air (gray). Solid lines are fits to $\exp[-(t/T_2)^\beta]$ with $\beta \approx 0.47$ in each case. Data normalized to the maximum N-V spin contrast. (b) Hahn echo decays for the same targets, showing a similar T_2 trend. Here τ is defined as the total length of the sequence. Solid lines are fits to single exponential decays.

APPENDIX C: PROTOCOL COMPARISON

As discussed in the main text, the PulsePol protocol is selected for this work due to its suitability in addressing a N-V ensemble over a wide field of view. To illustrate this, we compared the behavior of PulsePol and the well-known NOVEL sequence [55], depicted in Fig. 8(a), over an identical region [Fig. 8(b)] with biphenyl as the hydrogen target. Panels (c) and (e) show the appearance of the hydrogen resonance using the NOVEL and PulsePol sequences, respectively, with red and blue traces showing data averaged over the pixels contained within the corresponding regions marked on the N-V PL image (b). The NOVEL spectra are obtained by using a spin locking time of 20 μ s and sweeping the microwave power, which corresponds to a Rabi frequency in the rotating frame. The hydrogen resonance appears when, locally, the Rabi frequency matches the hydrogen Larmor frequency and indicates the transfer of spin polarization from N-V to the hydrogen bath. A microwave power gradient across our FOV results in the resonance appearing for different nominal driving powers between the two regions. Fitting the position of the resonance for every pixel in the image, shown in panel (d), confirms that there is a sharp gradient in resonance position across the whole FOV, meaning that it is impossible to transfer polarization using more than 1% of this region at any one time under our experimental conditions.

On the contrary, the spectra in Fig. 8(e) overlap, and the colorplot Fig. 8(f) confirms that the PulsePol resonance

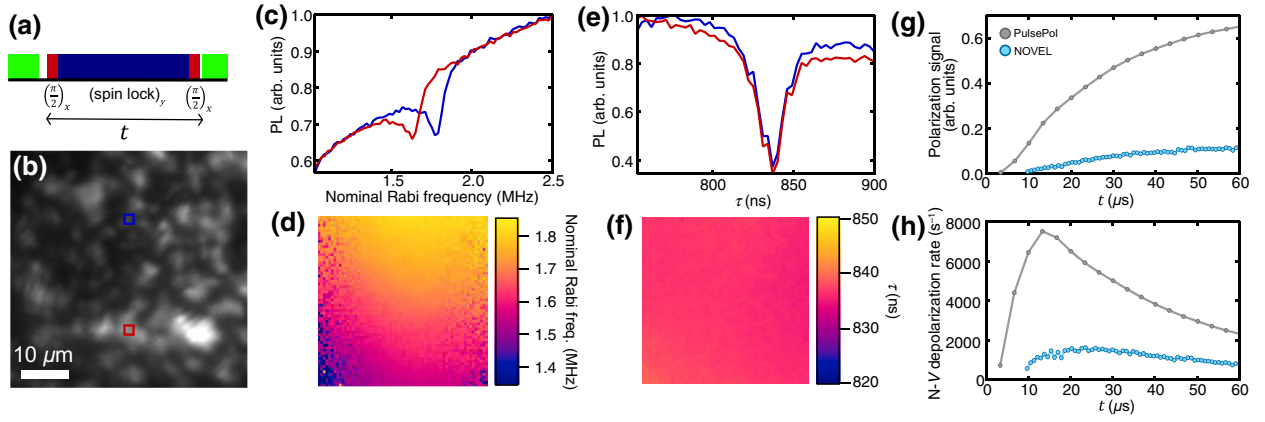


FIG. 8. (a) NOVEL pulse sequence schematic. (b) N- V PL image of $50 \times 50 \mu\text{m}^2$ FOV with areas for comparison highlighted by blue and red squares. (c) Spectra obtained using NOVEL with spin locking time $t = 20 \mu\text{s}$ showing hydrogen resonances (biphenyl). Red and blue traces are data obtained over the regions highlighted by red and blue squares in (b), respectively. (d) Colormap of the full $50 \times 50 \mu\text{m}^2$ FOV showing the position of hydrogen resonance at each pixel, given by fitting to a Lorentzian dip shape. (e) Same as (c) but for a τ sweep using the PulsePol sequence as defined in the main text ($N = 30$). (f) Colormap of the PulsePol hydrogen resonance position, fit as in (d). (g) Polarization signal normalized to background N- V decoherence obtained using PulsePol (gray) and NOVEL (light blue). NOVEL data taken over an approximate $2 \times 2 \mu\text{m}^2$ region while PulsePol data are averaged over the full FOV. (h) Cooling rates obtained (using the same definition as in the main text) using PulsePol (gray) and NOVEL (light blue).

position does not vary by more than its linewidth across the entire FOV, owing to the sequence's robustness to microwave power detuning. This fact allows all measurements in the main text to be taken as an average over the full FOV. The PulsePol resonances are also much deeper, corresponding to more efficient polarization transfer, despite the theoretical effective coupling being reduced by 28% compared to NOVEL. This is due to the fact that PulsePol achieves $T_2 > 20 \mu\text{s}$ whereas resonant $T_{1\rho} \approx 2 \mu\text{s}$ with $B \sim 430$ G. It is also possible that even the power gradient over a single micrometre scale is enough to reduce the efficiency of transfer using NOVEL.

Figures 8(g) and 8(h) show the difference between off- and on-resonance N- V decay, normalized to the background decoherence and converted to a cooling rate, respectively, for the two sequences (PulsePol shown in gray and NOVEL in light blue). As in the main text, the PulsePol signal is averaged over the entire FOV while the NOVEL signal is averaged over only the blue region. The influence of the longer PulsePol T_2 is clear, with much more efficient polarization transfer obtained per N- V with PulsePol than with NOVEL. The maximum cooling rate per N- V obtained using NOVEL is 1604 spins/sec, 79% less than that obtained using PulsePol. Again, assuming a proportionality between these values and the theoretical strong-dephasing cooling rate and recalling that $A_0(\text{PulsePol}) = 0.72A_0(\text{NOVEL})$ suggests that $T_{1\rho} < T_2^{\text{PP}}/10$, in agreement with the measured values.

Considering that NOVEL is only active over approximately 1% of the FOV, the steady-state hydrogen polarization possible to be enacted using this sequence in

our experiment is likely to be approximately 3 orders of magnitude lower than that obtained using PulsePol.

APPENDIX D: INFLUENCE OF SURFACE SPINS

The theoretical predictions in Figs. 2(c) and 2(d) are calculated by numerically integrating over a cubic volume with side length 30 nm, located 6 nm above a single N- V , and filled with hydrogen spins at a density $\rho_{\text{H}} = 41 \text{ nm}^{-3}$ set to that of biphenyl. For the coherent limit, only the total dipole-dipole coupling between the N- V and the hydrogen spin bath (A_0) needs to be calculated, while in the strong-dephasing limit (and our phenomenological hybrid model) the total dephasing rate $\Gamma_2^{\text{tot}} = \Gamma_2^{\text{N-}V} + \Gamma_2^{\text{H}}$ also needs to be calculated at each step in the integration as the polarization dynamics are set by the quantity $A_0^2/\Gamma_2^{\text{tot}}$, the strong-dephasing N- V depolarization rate. The rate $\Gamma_2^{\text{N-}V}$ is an experimentally accessible constant; however, Γ_2^{H} is expected to vary sharply with hydrogen distance from the diamond surface due to interactions with surface electron spins [23]. Therefore, for each hydrogen spin, we calculate $\Gamma_2^{\text{H}} = \Gamma_{2,\text{bulk}}^{\text{H}} + \Gamma_{2,\text{SS}}^{\text{H}}$, where $\Gamma_{2,\text{bulk}}^{\text{H}}$ is the bulk dephasing rate, unaffected by interactions with surface spins, and $\Gamma_{2,\text{SS}}^{\text{H}}$ is the contribution from the surface spins. The rate $\Gamma_{2,\text{bulk}}^{\text{H}}$ is found experimentally through XY8-64 correlation spectroscopy, fitting for wait times greater than $2 \mu\text{s}$ to only extract the longer bulk timescale. With the magnetic bias field oriented along the N- V axis, the contribution due to surface spins is given by

$$\Gamma_{2,\text{SS}}^{\text{H}} = 5.65 \frac{\mu_0 \hbar \gamma_e \gamma_{\text{H}} \sqrt{3\pi\sigma_e}}{64\pi h^2}, \quad (\text{D1})$$

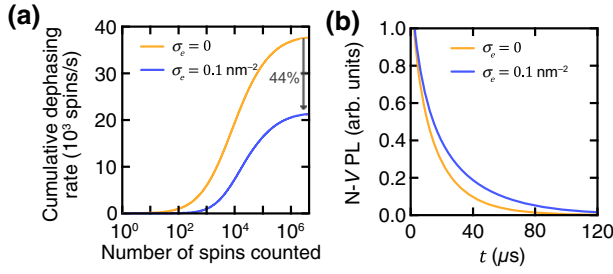


FIG. 9. (a) Calculation of the theoretical N- V dephasing rate in the strong-dephasing limit, $A_0^2/\Gamma_2^{\text{tot}}$, by numerical integration over a cubic volume with side length 30 nm, for surface electron spin densities of $\sigma_e = 0$ (orange) and $\sigma_e = 0.1 \text{ nm}^{-2}$ (blue). Contributions from hydrogen spins are added in order of descending raw coupling A_0 , so that those spins closest to the diamond surface are added first. A 44% reduction is found for the $\sigma_e = 0.1 \text{ nm}^{-2}$ case compared to $\sigma_e = 0$ when the full volume is summed over. (b) Theoretical resonant N- V decoherence curves in the strong-dephasing limit [Eq. (3)] predicted by the two numerically integrated quantities from (a). Without taking the dephasing due to the surface spins into account (orange curve), a more rapid decay is predicted. The slower decay predicted by taking $\sigma_e = 0.1 \text{ nm}^{-2}$ (blue) matches experimental data better [cf. Fig. 2(c)].

where μ_0 is the permeability of free space, γ_e and γ_H are the electron and hydrogen gyromagnetic ratios, respectively, h is the distance above the diamond surface, and σ_e is the areal density of electron spins on the diamond surface [23].

Figure 9(a) shows the effect of varying σ_e on the numerical integration of the strong-dephasing N- V depolarization rate $A_0^2/\Gamma_2^{\text{tot}}$. Choosing a realistic surface spin density of 0.1 nm^{-2} greatly reduces the interaction between N- V and the nearest hydrogen spins, ultimately resulting in an overall 44% reduction in polarization transfer as compared to the $\sigma_e = 0$ case.

Figure 9(b) shows the effect of this difference on the predicted N- V response, showing the strong-dephasing limit [Eq. (3)] for simplicity. Ignoring the contribution from the surface spins results in a more rapid N- V decay (and hence more efficient polarization transfer) compared to the realistic $\sigma_e = 0.1 \text{ nm}^{-2}$ case. In Figs. 2(c) and 2(d) we showed good agreement between experimental data and the $\sigma_e = 0.1 \text{ nm}^{-2}$ prediction, indicating the importance of including this term.

APPENDIX E: DIFFUSION DATA

In Sec. IIC we presented data showing the reduction in polarization transfer efficiency associated with increasing levels of molecular diffusion. Because of the uncertainty and potential inconsistency in reporting diffusion constants D_n for different targets, we presented that data only in terms of the kinematic viscosity (readily available in the literature for glycerol mixtures and provided

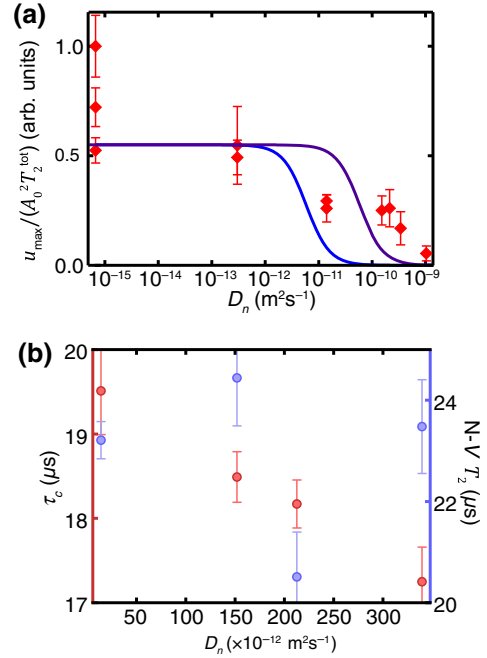


FIG. 10. (a) Normalized cooling rate plotted against the diffusion constant D_n . Solid lines show a theoretical prediction for N- V -H distances of 7 nm (blue) and 14 nm (purple). (b) Variation of correlation time τ_c measured by XY8-64 correlation spectroscopy (red points, left axis) and N- V PulsePol T_2 (blue points, right axis) for glycerol and water mixtures with $\chi_g = 1, 0.88, 0.75, 0.5$. Error bars show the standard fitting error. The diffusion constant D_n is given by Eq. (2) in Ref. [44].

by the manufacturer for viscous oil). For completeness, we plot the same data as in the main text against estimated values of D_n in Fig. 10(a). For the glycerol mixtures, we take values from the empirically derived formula in Ref. [44], while in the absence of manufacturer specification of molecular mass or hydrodynamic radius for the viscous oil, we use a value $D_n = 3 \times 10^{-13} \text{ m}^2 \text{ s}^{-1}$ estimated in previous work for a similar viscous oil [38]. With blue and purple solid lines we plot the curve $\tau_D^2/(\tau_D^2 + \tau_L^2)$ for N- V -H distances 7 and 14 nm, respectively, representing the approximate bounds of the N- V sensing volume. This equation gives the expected reduction in effective coupling to the hydrogen spin bath as a result of using the PulsePol sequence [23], which should be the only remaining diffusion-dependent factor following the normalization described in the main text. The maximum value is set arbitrarily, to match the solid target providing the least signal for illustration.

We can see some qualitative agreement between experiment and theory, with the viscous oil diffusing slowly enough to not be greatly affected, while a relatively rapid drop-off in effective coupling is observed for $\chi_g \leq 0.75$. However, overall the points belonging to the glycerol and water mixture series are not well described by the theory. As mentioned in the main text, two possible adjustments to

these data points could recover the expected trend: either a systematic decrease in D_n of around one order of magnitude due to interactions between the diamond surface and the fluid, or a less dramatic increase in diffusivity near the surface with decreasing χ_g . The latter case could arise due to the local properties of the mixtures changing near the surface, for instance due to laser heating causing water to evaporate, leaving $\chi_g > 0.9$ within the N-V sensing volume in all cases.

Support for both interpretations is found in experimental measurements of the bath correlation time via XY8-64 correlation spectroscopy [38], presented in Fig. 10(b) (red points, left axis), where we show only data for the glycerol mixture series (excluding pure water that gives a very poor signal). The correlation time τ_c varies inversely with D_n as expected, but not as sharply as predicted. Assuming that $T_2^* \gg T_2^{\text{diff}} \approx \tau_c$, we expect D_n^{-1} scaling, implying that D varies by less than 20% between $\chi_g = 1$ and $\chi_g = 0.5$. This would be consistent with a water evaporation effect, increasing the near surface χ_g . Additionally, taking the expression $\tau_c = 2d_{\text{N-V}}^2/D_n$ [53] and $\tau_c = 19.51 \mu\text{s}$ obtained for pure glycerol gives $D_n = 3.69 \times 10^{-12} \text{ m}^2 \text{ s}^{-1}$ (for $d_{\text{N-V}} = 6 \text{ nm}$), well below the literature value.

-
- [1] A. Abragam and M. Goldman, Principles of dynamic nuclear polarisation, *Rep. Prog. Phys.* **41**, 395 (1978).
- [2] R. A. Wind, M. J. Duljvestlin, C. V. D. L. Lugt, and J. Vriend, Applications of dynamic nuclear polarization in ^{13}C NMR in solids, *Prog. NMR Spectrosc.* **17**, 33 (1985).
- [3] D. A. Hall, D. C. Maus, G. J. Gerfen, S. J. Inati, L. R. Becerra, F. W. Dahlquist, and R. G. Griffin, Polarization-enhanced NMR spectroscopy of biomolecules in frozen solution, *Science* **276**, 930 (1997).
- [4] K. Tateishi, M. Negoro, S. Nishida, A. Kagawa, and Y. Morita, Room temperature hyperpolarization of nuclear spins in bulk, *PNAS* **111**, 21 (2014).
- [5] J. Natterer and J. Bargon, Parahydrogen induced polarization, *Prog. Nucl. Magn. Reson. Spectrosc.* **31**, 293 (1997).
- [6] J.-B. Hövener, A. N. Pravdivtsev, B. Kidd, C. R. Bowers, S. Glöggler, K. V. Kovtunov, M. Plaumann, R. Katz-brull, K. Buckenmaier, A. Jerschow, *et al.*, Parahydrogen-based hyperpolarization for biomedicine angewandte, *Angew. Chem. Int. Ed.* **57**, 11140 (2018).
- [7] T. G. Walker and W. Happer, Spin-exchange optical pumping of noble-gas nuclei, *Rev. Mod. Phys.* **69**, 2 (1997).
- [8] G. Navon, Y. Song, S. Appelt, R. E. Taylor, and A. Pinest, Enhancement of solution NMR and MRI with laser-polarized xenon, *Science* **271**, 5257 (1996).
- [9] M. W. Doherty, N. B. Manson, P. Delaney, F. Jelezko, J. Wrachtrup, and L. C. Hollenberg, The nitrogen-vacancy colour centre in diamond, *Phys. Rep.* **528**, 1 (2013).
- [10] D. A. Broadway, J.-P. Tetienne, A. Stacey, J. D. A. Wood, D. A. Simpson, L. T. Hall, and L. C. L. Hollenberg, Quantum probe hyperpolarisation of molecular nuclear spins, *Nat. Commun.* **9**, 1246 (2018).
- [11] P. Fernandez-Acebal, O. Rosolio, J. Scheuer, C. Muller, S. Muller, S. Schmitt, L. P. McGuinness, I. Schwarz, W. Chen, A. Retzker, *et al.*, Toward hyperpolarization of oil molecules via single nitrogen vacancy centers in diamond, *Nano Lett.* **18**, 1882 (2018).
- [12] F. Shagieva, S. Zaiser, D. B. R. Dasari, R. Stohr, A. Denisenko, R. Reuter, C. A. Meriles, and J. Wrachtrup, Microwave-assisted cross-polarization of nuclear spin ensembles from optically pumped nitrogen-vacancy centers in diamond, *Nano Lett.* **18**, 3731 (2018).
- [13] P. London, J. Scheuer, J. Cai, I. Schwarz, A. Retzker, M. B. Plenio, M. Katagiri, T. Teraji, S. Koizumi, J. Isoya, *et al.*, Detecting and Polarizing Nuclear Spins with Double Resonance on a Single Electron Spin, *Phys. Rev. Lett.* **111**, 067601 (2013).
- [14] J. P. King, P. J. Coles, and J. A. Reimer, Optical polarization of ^{13}C nuclei in diamond through nitrogen vacancy centers, *Phys. Rev. B* **81**, 073201 (2010).
- [15] D. Pagliero, K. R. K. Rao, P. R. Zangara, S. Dhomkar, H. H. Wong, A. Abril, N. Aslam, A. Parker, J. King, C. E. Avalos, *et al.*, Multispin-assisted optical pumping of bulk ^{13}C nuclear spin polarization in diamond, *Phys. Rev. B* **97**, 024422 (2018).
- [16] A. Ajoy, K. Liu, R. Nazaryan, X. Lv, P. R. Zangara, B. Savvati, G. Wang, D. Arnold, G. Li, A. Lin, *et al.*, Orientation-independent room temperature optical ^{13}C hyperpolarization in powdered diamond, *Sci. Adv.* **4**, eaar5492 (2018).
- [17] J. Henshaw, D. Pagliero, P. R. Zangara, M. B. Franzoni, A. Ajoy, and R. H. Acosta, Carbon-13 dynamic nuclear polarization in diamond via a microwave-free integrated cross effect, *PNAS* **116**, 37 (2019).
- [18] I. Schwartz, J. Scheuer, B. Tratzmiller, S. Müller, Q. Chen, I. Dhand, Z.-Y. Wang, C. Muller, B. Naydenov, F. Jelezko, *et al.*, Robust optical polarization of nuclear spin baths using Hamiltonian engineering of nitrogen-vacancy center quantum dynamics, *Sci. Adv.* **4**, eaar8978 (2018).
- [19] J. E. Lang, D. A. Broadway, G. A. L. White, L. T. Hall, A. Stacey, L. C. L. Hollenberg, T. S. Monteiro, and J. P. Tetienne, Quantum Bath Control with Nuclear Spin State Selectivity Via Pulse-Adjusted Dynamical Decoupling, *Phys. Rev. Lett.* **123**, 210401 (2019).
- [20] J.-P. Tetienne, L. T. Hall, A. J. Healey, G. A. L. White, M.-A. Sani, F. Separovic, and L. C. L. Hollenberg, Prospects for nuclear spin hyperpolarization of molecular samples using nitrogen-vacancy centers in diamond, *Phys. Rev. B* **103**, 014434 (2021).
- [21] D. R. Glenn, D. B. Bucher, J. Lee, M. D. Lukin, H. Park, and R. L. Walsworth, High-resolution magnetic resonance spectroscopy using a solid-state spin sensor, *Nature* **555**, 7696 (2018).
- [22] J. Smits, J. Damron, P. Kehayias, A. F. McDowell, N. Mosavian, I. Fescenko, N. Ristoff, A. Laraoui, A. Jarmola, and V. M. Acosta, Two-dimensional nuclear magnetic resonance spectroscopy with a microfluidic diamond quantum sensor, *Sci. Adv.* **5**, eaaw7895 (2019).
- [23] L. T. Hall, D. A. Broadway, A. Stacey, D. A. Simpson, J.-P. Tetienne, and L. C. L. Hollenberg, *arXiv:2012.12508* (2020).
- [24] E. Bauch, S. Singh, J. Lee, C. A. Hart, J. M. Schloss, M. J. Turner, J. F. Barry, L. Pham, N. Bar-gill, S. F. Yelin, *et al.*, Decoherence of ensembles of nitrogen-vacancy centers in diamond, *Phys. Rev. B* **102**, 134210 (2020).

- [25] S. Pezzagna, B. Naydenov, F. Jelezko, J. Wrachtrup, and J. Meijer, Creation efficiency of nitrogen-vacancy centres in diamond, *New J. Phys.* **12**, 065017 (2010).
- [26] A. Stacey, N. Dontschuk, J.-P. Chou, D. A. Broadway, A. K. Schenk, M. J. Sear, J.-P. Tetienne, A. Hoffman, S. Prawer, C. I. Pakes, *et al.*, Evidence for primal sp^2 defects at the diamond surface: Candidates for electron trapping and noise sources, *Adv. Mater. Interfaces* **6**, 3 (2019).
- [27] T. Roskopf, A. Dussaux, K. Ohashi, M. Loretz, R. Schirhagl, H. Watanabe, S. Shikata, K. M. Itoh, and C. L. Degen, Investigation of Surface Magnetic Noise by Shallow Spins in Diamond, *Phys. Rev. Lett.* **112**, 147602 (2014).
- [28] B. A. Myers, A. Das, M. C. Dartiaill, K. Ohno, D. D. Awschalom, and A. C. Bleszynski Jayich, Probing Surface Noise with Depth-Calibrated Spins in Diamond, *Phys. Rev. Lett.* **113**, 027602 (2014).
- [29] Y. Romach, C. Müller, T. Uden, L. J. Rogers, T. Isoda, K. M. Itoh, M. Markham, A. Stacey, J. Meijer, S. Pezzagna, *et al.*, Spectroscopy of Surface-Induced Noise Using Shallow Spins in Diamond, *Phys. Rev. Lett.* **114**, 017601 (2015).
- [30] D. Bluvstein, Z. Zhang, and A. C. B. Jayich, Identifying and Mitigating Charge Instabilities in Shallow Diamond Nitrogen-Vacancy Centers, *Phys. Rev. Lett.* **122**, 76101 (2019).
- [31] J. P. Tetienne, R. W. De Gille, D. A. Broadway, T. Teraji, S. E. Lillie, J. M. McCoe, N. Dontschuk, L. T. Hall, A. Stacey, D. A. Simpson, *et al.*, Spin properties of dense near-surface ensembles of nitrogen-vacancy centers in diamond, *Phys. Rev. B* **97**, 085402 (2018).
- [32] L. T. Hall, P. Kehayias, D. A. Simpson, A. Jarmola, A. Stacey, D. Budker, and L. C. Hollenberg, Detection of nanoscale electron spin resonance spectra demonstrated using nitrogen-vacancy centre probes in diamond, *Nat. Commun.* **7**, 10211 (2016).
- [33] T. T. P. Cheung, Spin diffusion in NMR in solids, *Phys. Rev. B* **23**, 3 (1981).
- [34] S.-B. Liu and M. S. Conradi, Excitation in Incommensurate Biphenyl: Proton Spin-Lattice Relaxation, *Phys. Rev. Lett.* **54**, 12 (1985).
- [35] M. Kim, H. J. Mamin, M. H. Sherwood, K. Ohno, D. D. Awschalom, and D. Rugar, Decoherence of Near-Surface Nitrogen-Vacancy Centers Due to Electric Field Noise, *Phys. Rev. Lett.* **115**, 087692 (2015).
- [36] M. Mamatkulov, L. Stauffer, C. Minot, and P. Sonnet, Ab initio study of biphenyl chemisorption on Si (001): Configurational stability, *Phys. Rev. B* **73**, 035321 (2006).
- [37] M. Dubois, C. Delerue, and A. Rubio, Adsorption and electronic excitation of biphenyl on Si (100): A theoretical STM analysis, *Phys. Rev. B* **75**, 041302 (2007).
- [38] T. Staudacher, N. Raatz, S. Pezzagna, J. Meijer, F. Reinhard, J. Wrachtrup, and C. A. Meriles, Probing molecular dynamics at the nanoscale via an individual paramagnetic centre, *Nat. Commun.* **6**, 8572 (2015).
- [39] S. J. Devience, L. M. Pham, I. Lovchinsky, A. O. Sushkov, N. Bar-gill, C. Belthangady, F. Casola, M. Corbett, H. Zhang, M. Lukin, *et al.*, Nanoscale NMR spectroscopy and imaging of multiple nuclear species, *Nat. Nanotechnol.* **10**, 129 (2015).
- [40] P. Berthault, C. Boutin, C. Martineau-corcous, and G. Carret, Progress in nuclear magnetic resonance spectroscopy use of dissolved hyperpolarized species in NMR: Practical considerations, *Prog. Nucl. Magn. Reson. Spectrosc.* **118–119**, 74 (2020).
- [41] D. B. Bucher, D. R. Glenn, H. Park, M. D. Lukin, and R. L. Walsworth, Hyperpolarization-Enhanced NMR Spectroscopy with Femtomole Sensitivity Using Quantum Defects in Diamond, *Phys. Rev. X* **10**, 021053 (2020).
- [42] N. Arunkumar, D. B. Bucher, M. J. Turner, P. Tomhoh, D. Glenn, S. Lehmkühl, M. D. Lukin, H. Park, M. S. Rosen, T. Theis, *et al.*, Micron-scale NV-NMR spectroscopy with signal amplification by reversible exchange, *PRX Quantum* **2**, 010305 (2021).
- [43] A. Volk and C. J. Kähler, Density model for aqueous glycerol solutions, *Exp. Fluids* **59**, 5 (2018).
- [44] G. D’Errico, O. Ortona, F. Capuano, V. Vitagliano, F. Ii, and V. Cinthia, Diffusion coefficients for the binary system glycerol + water at 25°C. A velocity correlation study, *J. Chem. Eng. Data* **49**, 6 (2004).
- [45] A. J. Healey, A. Stacey, B. C. Johnson, D. A. Broadway, T. Teraji, D. A. Simpson, J. Tetienne, and L. C. L. Hollenberg, Comparison of different methods of nitrogen-vacancy layer formation in diamond for wide-field quantum microscopy, *Phys. Rev. Mater.* **4**, 104605 (2020).
- [46] T. Lühmann, R. John, R. Wunderlich, J. Meijer, and S. Pezzagna, Coulomb-driven single defect engineering for scalable qubits and spin sensors in diamond, *Nat. Commun.* **10**, 4956 (2019).
- [47] S. Sangtawesin, B. L. Dwyer, S. Srinivasan, J. J. Allred, L. V. H. Rodgers, K. D. Greve, A. Stacey, N. Dontschuk, K. M. O. Donnell, D. Hu, *et al.*, Origins of Diamond Surface Noise Probed by Correlating Single-Spin Measurements with Surface Spectroscopy, *Phys. Rev. X* **8**, 031052 (2019).
- [48] D. Tauber and C. von Borczyskowski, Single molecule studies on dynamics in liquid crystals, *Int. J. Mol. Sci.* **14**, 19506 (2013).
- [49] H. C. Gaede and K. Gawrisch, Lateral diffusion rates of lipid, water, and a hydrophobic drug in a multilamellar liposome, *Biophys. J.* **85**, 3 (2003).
- [50] D. A. Broadway, J. D. A. Wood, L. T. Hall, A. Stacey, M. Markham, D. A. Simpson, J. P. Tetienne, and L. C. L. Hollenberg, Anticrossing Spin Dynamics of Diamond Nitrogen-Vacancy Centers and All-Optical Low-Frequency Magnetometry, *Phys. Rev. Appl.* **6**, 064001 (2016).
- [51] T. Teraji, High-quality and high-purity homoepitaxial diamond (100) film growth under high oxygen concentration condition, *J. Appl. Phys.* **118**, 115304 (2015).
- [52] M. Loretz, J. M. Boss, T. Roskopf, H. J. Mamin, D. Rugar, and C. L. Degen, Spurious Harmonic Response of Multi-pulse Quantum Sensing Sequences, *Phys. Rev. X* **5**, 021009 (2015).
- [53] L. M. Pham, S. J. Devience, F. Casola, I. Lovchinsky, A. O. Sushkov, E. Bersin, J. Lee, E. Urbach, P. Cappellaro, H. Park, *et al.*, NMR technique for determining the depth of shallow nitrogen-vacancy centers in diamond, *Phys. Rev. B* **93**, 045425 (2016).
- [54] F. Ziem, M. Garsi, H. Fedder, and J. Wrachtrup, Quantitative nanoscale MRI with a wide field of view, *Sci. Rep.* **9**, 12166 (2019).
- [55] A. Henstra and W. T. Wenckebach, The theory of nuclear orientation via electron spin locking (NOVEL), *Mol. Phys.* **106**, 7 (2008).